

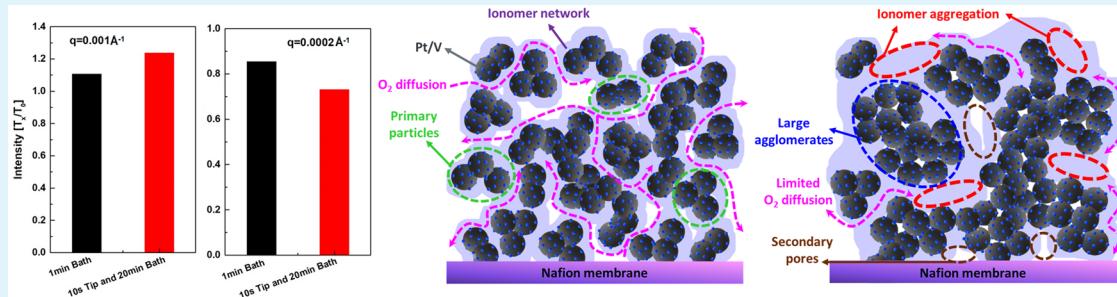
Impact of Catalyst Ink Dispersing Methodology on Fuel Cell Performance Using in-Situ X-ray Scattering

Min Wang,^{†,‡,§} Jae Hyung Park,^{‡,§} Sadia Kabir,[†] K. C. Neyerlin,^{†,§} Nancy N. Kariuki,[‡] Haifeng Lv,[§] Vojislav R. Stamenkovic,[§] Deborah J. Myers,[‡] Michael Ulsh,[†] and Scott A. Mauger^{*,†,§}

[†]Chemistry and Nanoscience Center, National Renewable Energy Laboratory, 15013 Denver West Parkway, Golden, Colorado 80401, United States

[‡]Chemical Sciences and Engineering Division and [§]Materials Science Divisions, Argonne National Laboratory, Argonne, Illinois 60439, United States

Supporting Information



ABSTRACT: This work presents a study of the effects of ultrasonic dispersing methodology and time on catalyst agglomerate size in polymer electrolyte membrane fuel cell (PEMFC) catalyst ink dispersions. Cathode catalyst inks were prepared and characterized to elucidate the influences of ultrasonic dispersing method and time on catalyst ink particle size and CCL electrochemical properties. In-situ ultra-small-, small-, and wide-angle X-ray scattering (USAXS–SAXS–WAXS) analyses were used to study the impact of ultrasonication time and methodology on changes in the agglomerate, aggregate, and particle size and distribution during the dispersing process. Ex-situ transmission electron microscopy was also used to investigate the particle size of these inks. Fuel cell membrane electrode assemblies (MEAs) were prepared and tested to determine the influence of ink properties on CCL electrochemical properties, including the electrochemical active surface area (ECA), mass activity (MA), H₂/air polarization curves, and oxygen mass-transport resistances. It was found that a combination of brief tip sonication followed by bath sonication was most effective at breaking up agglomerates, leading to maximum catalyst activity and MEA performance. Extended tip sonication was found to be too aggressive and resulted in detachment of the platinum nanoparticles from the carbon black support, which decreased electrochemical surface area and MEA performance. Quantification of oxygen mass transport resistance showed that electrodes with large catalyst agglomerates due to insufficient sonication had a higher non-Fickian (pressure independent) than properly dispersed catalyst. Through correlation of the performance with catalyst particle size, the desired CCL structure was proposed, which will provide insight into dispersion strategies for lab-scale spray coating and other processing techniques as well as for large-scale manufacturing.

KEYWORDS: catalyst ink, dispersing, in-situ X-ray scattering, USAXS, particle size, proton-exchange membrane fuel cells

1. INTRODUCTION

Polymer electrolyte membrane fuel cells (PEMFCs) are an efficient and environmentally friendly energy conversion technology that have great potential to reduce or replace the use of fossil fuels in a number of applications, most notably in automobiles. In a PEMFC, H₂ and O₂ are supplied as the reactants at the anode and cathode, respectively, while the electrochemical reaction energy is converted to electricity and heat. Because the oxygen reduction reaction (ORR) has relatively sluggish kinetics, numerous PEMFC studies have focused on developing high-performance cathodes through development and optimization of catalyst materials¹ and electrode structure.² In the membrane electrode assembly

(MEA), the cathode catalyst layer (CCL) is a very important component that has a major impact on the cell performance and lifetime.³ Catalyst layers are typically composed of a platinum-based nanoparticle catalyst supported on a high-surface-area carbon support material, ionomer, and primary and secondary pores.⁴ The CCL is typically applied directly to the membrane or onto a substrate to form a decal that is transferred to the membrane to form a catalyst-coated membrane (CCM) or onto the gas-diffusion layer to form a

Received: May 24, 2019

Accepted: July 26, 2019

Published: July 26, 2019

gas-diffusion electrode (GDE) that is hot-pressed to the membrane to form the MEA. The CCL is formed by different solution-coating methods, including hand painting, air brushing, ultrasonic spray coating, Mayer rod coating, or large-scale roll-to-roll (R2R) coating.^{5–8} The catalyst ink formulation and processing must be adjusted to achieve the ink properties required to form an adherent and continuous layer, as defined by the physics of each different coating process. In particular, ink processing is known to have a large impact on the catalyst ink viscosity, the interaction between the catalyst and ionomer, the catalyst particle size,⁹ catalyst utilization,¹⁰ CCL surface morphology and thickness, ionomer distribution, and the resulting cell performance.¹¹ Thus, it is necessary and important to understand (1) the relationship between ink processing techniques and the CCL particle size and structure and (2) how the particle size affects electrochemical performance at a device level. With the understanding of the desired catalyst particle size and CCL structure, we can provide guidance to develop ink processing techniques and formulations for efficient fabrication of electrodes, regardless of the coating methods.

As is well-known, the main purposes of ink processing are to break up agglomerates of catalyst/support aggregates to a desired size and to form a uniform ink dispersion for further electrode fabrication. In the case of Pt/C catalysts, the platinum nanoparticles (2–5 nm) are supported on conductive carbon blacks to achieve high utilization of the catalytically active sites. The microstructures of different carbon black supports such as Ketjenblack and Vulcan XC-72 have been studied extensively.¹² The carbon black primary particles (~20–40 nm) arrange into large fractal aggregates (100–300 nm). The aggregates have a propensity to cluster together to form predominant entities known as agglomerates (1–10 μm).^{13,14} Following coating, as the solvent is removed from the ink during drying, mesopores (2–20 nm) are formed within the aggregates and mesopores and macropores within and between the agglomerates (>20 nm).¹⁵ The agglomerate size has been shown to be important to CCL performance, and simulations have been utilized to aid in understanding this behavior.¹⁶

Effective ink processing is necessary to break up the large carbon agglomerates to achieve the desired particle size and ink viscosity for different coating methods. Typical processing methods include ball milling (also known as bead milling), high shear mixing, and ultrasonic homogenization (ultrasonic bath or probe). Ultrasonication has been widely used to enhance nanoscale dispersion by the destruction of agglomerates because of the unique action of ultrasonic waves and their high efficiency.^{9,17} Pollet et al. systematically investigated the properties of Pt/C catalyst inks (particle size and ECA) prepared from both ultrasonication and mechanical shear mixing and demonstrated the importance of ultrasonic parameters in the preparation of catalyst inks for rotating disk electrode (RDE) experiments.¹⁸ It was found that either a bath or probe ultrasonication was helpful for catalyst dispersion and maximizing catalytic activity; however, aggressive ultrasonication treatment resulted in lower ECA.¹⁸ This work was followed up a detailed review of sonochemistry, physical aspects of ultrasonication, equipment, and the impacts of ultrasound of fuel cell materials.¹⁹ Additionally, previous work conducted at the National Renewable Energy Laboratory showed that low sonication power and the use of an ice bath were important to maximize ECA and catalyst activity.²⁰

Sonication treatment in an ice bath environment was effective to avoid heating and sintering of the Pt nanoparticles.²⁰ In this work, we employed different types and time of ultrasonication to process the catalyst inks and performed an in-situ study of the catalyst particle size using X-ray scattering techniques to relate the catalyst ink structure to CCL performance in an MEA.

X-ray scattering analysis is a nondestructive analytic technique to study physical structures, chemical compositions, and crystal morphologies in nanomaterials with a wide range of length scales. X-ray scattering methods allow for high statistical information in the particle size distribution over the whole sample in a variety of sample types such as powders, solids, and liquids.²¹ While transmission electron microscopy (TEM) is widely used to study size distribution and shape of nanoparticles from direct images, it is only valid for local information at a certain position and does not provide the same level of statics as X-ray scattering. In this work we have used a combination of SAXS and USAXS. Pinhole SAXS data generally have information about size and structure at length scales of 1–20 nm constrained by the limits of the scattering angles detected. USAXS instruments can detect broader size ranges with dimensions above 1 μm .²² Combining WAXS with USAXS–SAXS (in a single instrument) measurements provides not only structural information such as particle size, shape, surface area, and volume from nanometer to micrometer size colloidal particles but also phase structure in a single scan. This instrument has been used to determine carbon–ionomer aggregate and agglomerate size distributions of electrocatalyst–ionomer inks and electrodes. The microstructural interaction between Nafion ionomer and carbon particle aggregates was previously studied by using the USAXS.^{23,24} A key feature of using a USAXS–SAXS–WAXS instrument is that it is possible to precisely determine the difference between primary particles and aggregates of the carbon ink dispersion.

In this study, ultrasonication and spray coating were applied to process the catalyst inks and fabricate electrodes. Both in-situ X-ray scattering and ex-situ TEM techniques were employed to investigate the particle size of these inks. The MEAs' electrochemical performance were comprehensively investigated in fuel cell tests to understand the structure–property relationship between catalyst particle size, electrode structure, mass transport behavior, and cell performance. Based on our results, the desired CCL structure was proposed, which will provide insight into dispersion strategies for different coating techniques.

2. EXPERIMENTAL SECTION

Materials. Two commercial Tanaka Kikinzoku Kogyo (TKK) Pt/C catalysts TEC10V50E (Pt/V, 47 wt % Pt) and TEC10E50E (Pt/HSC, 46.7 wt % Pt) were used at the cathode and anode, respectively. The Nafion dispersion (D2020, 1000EW at 20 wt %) was purchased from Ion Power. DuPont Nafion perfluorosulfonic acid (PFSA) NRE-211 membranes were employed in this study. The gas diffusion medium (GDM) was Sigracet 29 BC (SGL 29BC) with a 5% polytetrafluoroethylene (PTFE) microporous layer (MPL). OmniSolv *n*-propanol (*n*-PA) was HPLC grade from Millipore Sigma. Water was deionized and purified to a resistivity of 18.2 M Ω ·cm by using a Milli-Q system.

X-ray Scattering Characterization. USAXS–SAXS–WAXS measurements were performed at beamline 9ID-C at the Advanced Photon Source (APS) at Argonne National Laboratory. As shown in Figure S1, the premixed catalyst ink was loaded into a glass flask which was immersed in a bath sonicator filled with an ice–water

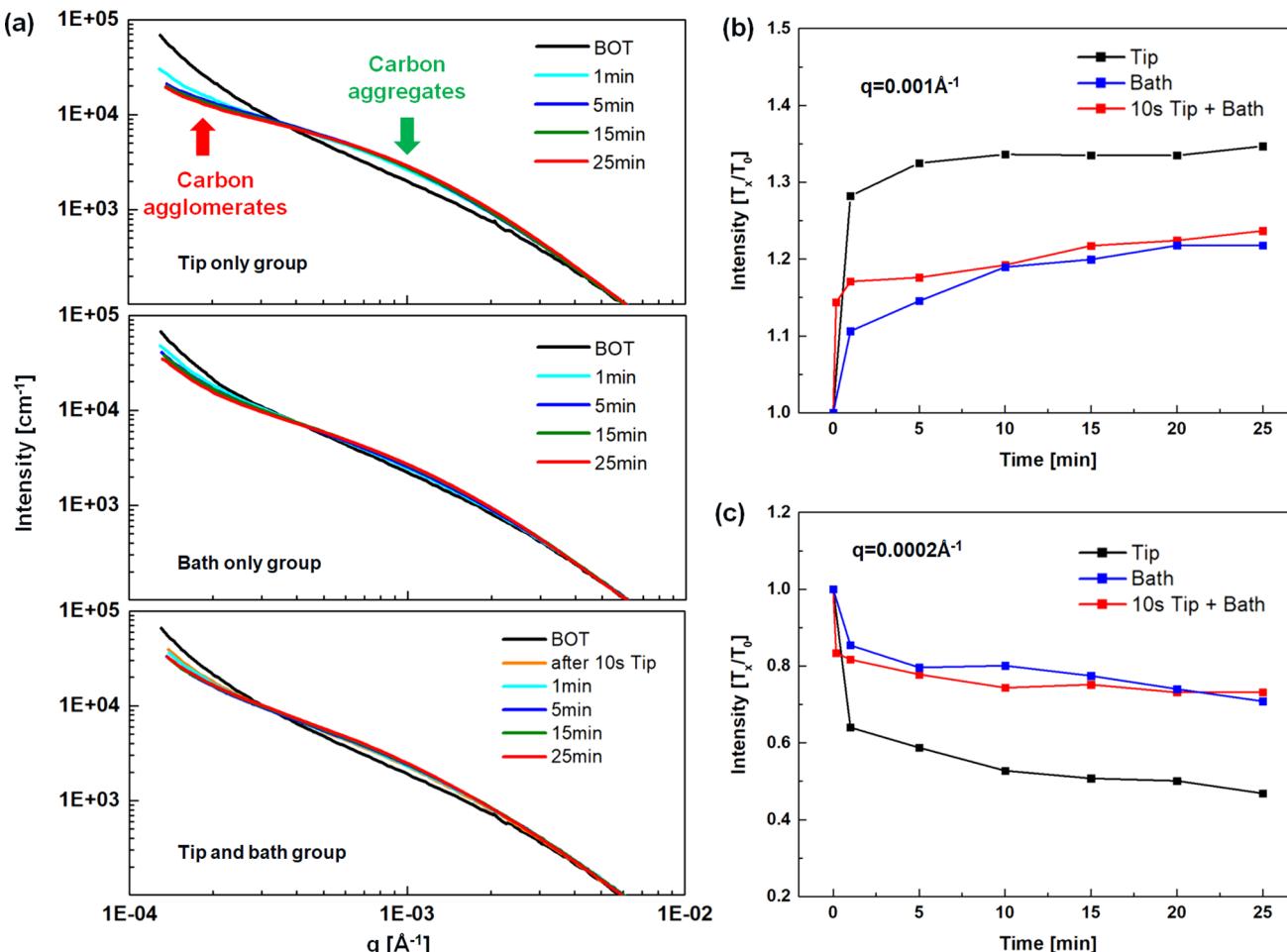


Figure 1. (a) USAXS profiles for Pt/Vulcan–ionomer–solvent inks as a function of sonication time processed by tip sonication, bath sonication, and tip/bath sonication plotted on log–log scales. The intensity values of USAXS spectra are normalized by the initial data (T_0) at (b) $q = 0.001\text{Å}^{-1}$ (aggregates region) and (c) $q = 0.0002\text{Å}^{-1}$ (agglomerates region). BOT: beginning of test.

mixture (Fisher Scientific FS30, 100 W). A horn sonicator tip (Branson Sonifer SFX250, 250 W; micro tip diameter: 3 mm) was immersed in the same ink and sealed onto the flask using a rubber cap. The catalyst ink was delivered to a 4 mm diameter glass tube in the X-ray beam path using a peristatic pump. The ink was delivered to the bottom of the capillary tube to completely fill the tube and prevent the formation of bubbles of air which can interfere with the X-ray scattering measurements. The flow rate was sufficiently high that the residence time of the liquid in the beam path was short enough to avoid any bubble formation. Additionally, the beam is unfocused and relatively large (0.8 mm × 0.8 mm), so even though the total photon flux is high, the flux density is relatively low, which also makes bubble formation unlikely. As the inks were passing through the capillary tube, they were exposed to a monochromatic X-ray beam in the range 16.8–21 keV. The scattered X-ray intensity was measured over the USAXS–SAXS–WAXS scattering angle ranges using a Bonse–Hart camera for USAXS and a Pilatus 100 K detector for pinhole SAXS and WAXS. The complete intensity data were collected in two scattering angle ranges of 10^{-4} – $6 \times 10^{-2}\text{ Å}^{-1}$ for the USAXS and 3×10^{-2} – 1 Å^{-1} for the pinhole SAXS. Therefore, these combined USAXS–SAXS–WAXS data correspond to length scales from 6 μm to 0.1 nm covering the size range of both mass fractal agglomerates and primary carbon black aggregates. The data were collected sequentially by using these two detectors with a time resolution of 5 min (WAXS and SAXS acquisition time was 30 s, and USAXS flyscan acquisition time was 90 s). The background scattering data from the capillary tube filled with the solvent solution (*n*-PA/water) were recorded and subtracted from scattering data for each catalyst ink. The raw data were reduced and

analyzed in the data analysis macro package Irena (Jan Ilavsky, APS, beamline 9ID-C) on the Igor Pro (WaveMetrics, OR) platform with fitting and simulations of scattering model functions.²⁵

Catalyst Ink Preparation. The cathode catalyst ink recipe is a mixture of Pt/V powders, D2020 ionomer dispersion, DI water, and *n*-PA with a Nafion/carbon weight ratio (I/C ratio) of 0.5 and H₂O/alcohol volume ratio of 1.3. The mixtures were then treated by pulsed tip sonication (output power: 15%; frequency: 4 s on and 8 s off) or bath sonication for 1, 5, and 20 min, respectively, noted as tip only group and bath only group. Another group was treated by 10 s continuous tip sonication and followed by bath sonication for 1, 5, and 20 min, noted as tip and bath group. All the sonication treatments were performed in an ice bath environment to avoid heating and sintering of the Pt nanoparticles. The anode catalyst ink was prepared by mixing the Pt/HSC powders, D2020 ionomer dispersion, DI water, and *n*-PA together with an I/C ratio of 0.9 and H₂O/alcohol volume ratio of 1.3. The mixture was first treated by tip sonication for 10 s, followed by ice bath sonication for another 20 min.

Structure Characterization. Transmission electron microscopy (TEM) images were acquired from a JEOL JEM2100F. For TEM sample preparation, 20 μL of the diluted cathode catalyst inks was drop-cast on the copper grids and dried at 50 °C in an ambient atmosphere.

MEA Fabrication. The CCMs were prepared by spray coating catalyst inks on each side of NRE 211 membranes using a Sono-tek ExactaCoat System with a 25 kHz AccuMist nozzle. Before spraying, the membranes were placed on a heated vacuum plate at ≈80 °C. The catalyst ink was then sprayed on the membrane in a 50 cm² square

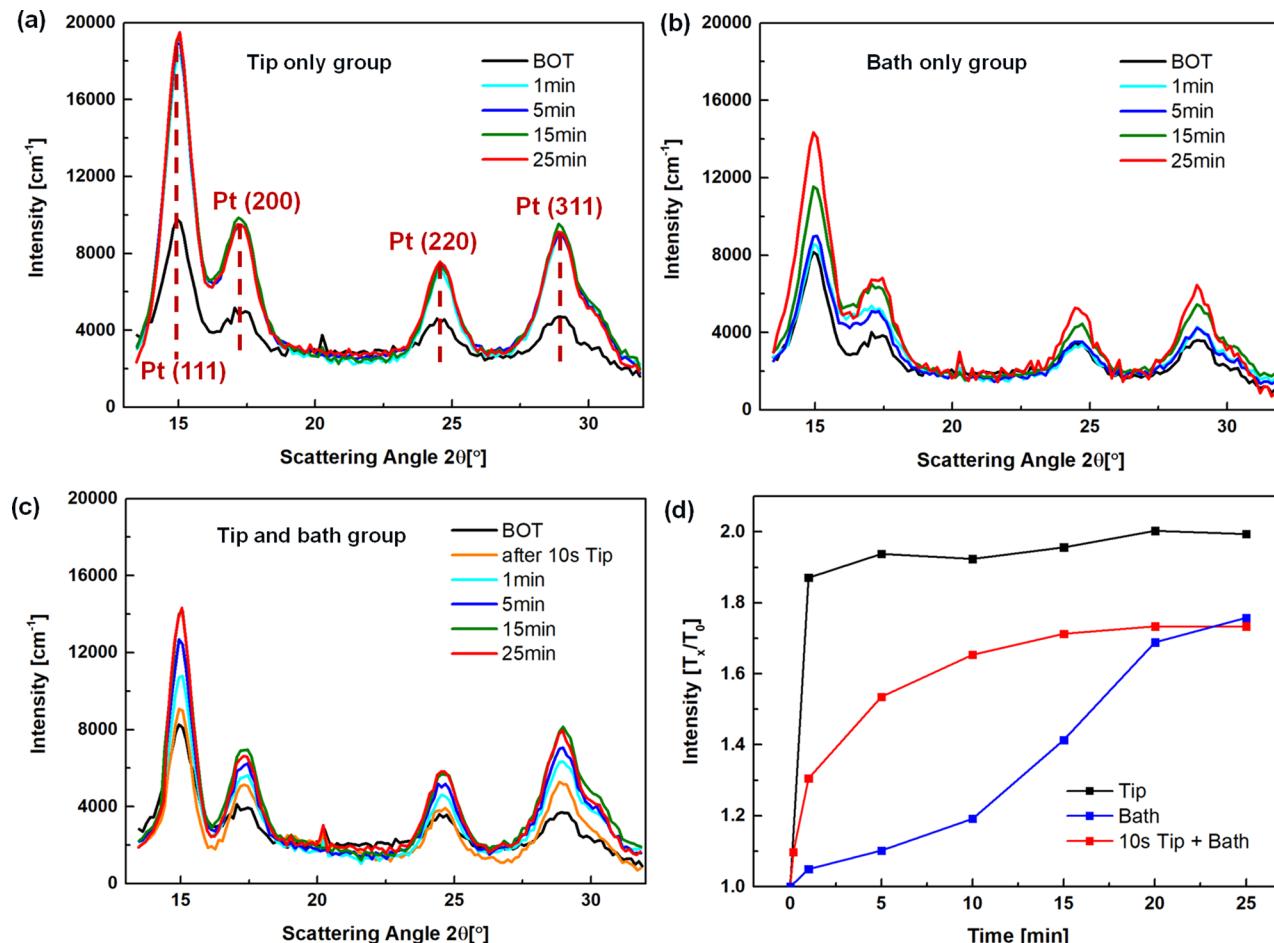


Figure 2. WAXS patterns for catalyst inks as a function of sonication time with different sonication methods: (a) tip, (b) bath, and (c) tip and bath. (d) Normalized WAXS intensity at scattering angle $2\theta = 15^\circ$. BOT: beginning of test.

area, denoted as the “active area”, at a pump rate of 0.3 mL/min. The desired cathode catalyst loading amount was $\approx 0.04 \text{ mg}_{\text{Pt}}/\text{cm}^2$. Low Pt loading was selected because O_2 transport behavior will be studied in our work to understand how the catalyst structure and particle size affect the mass transport. It has been previously shown that the non-Fickian O_2 transport resistance increases as electrode roughness factor ($\text{cm}^2_{\text{Pt}}/\text{cm}^2_{\text{MEA}}$) decreases.²⁶ Thus, decreasing the loading gives a stronger response and makes it easier to assess transport resistance differences between electrodes. Pt/V was selected as the cathode catalyst due to its simple support structure. In the case of Pt/V, the solid carbon support had very little internal porosity, and the Pt particles were located on the carbon exterior.²⁷ This eliminates the need to consider Knudsen diffusion in the internal carbon pores as a source of non-Fickian O_2 transport resistance. Therefore, the non-Fickian transport resistances will only be a function of ionomer thin film coverage and electrode secondary pore structure. The cathode catalyst loading amount was measured by XRF, checking nine fixed locations on the 50 cm^2 electrode, and the average value was used for the calculation of mass activity. The anode catalyst loading was $\approx 0.1 \text{ mg}_{\text{Pt}}/\text{cm}^2$. The as-prepared CCMs were assembled with two SGL 29BC GDMs by using two polytetrafluoroethylene (PTFE) gaskets into single fuel cell hardware with double/triple serpentine (anode/cathode) graphite flow fields. Gasket thickness was chosen to establish 25% GDL compression while assuming 6% gasket compression at a compression torque of 40 in. pounds.

Electrochemical Tests. Fuel cell testing was performed using a customized Hydrogenics test station. The protocols applied to all 50 cm^2 MEAs tested in this work consisted of a (i) break-in procedure followed by (ii) three voltage recovery cycles.⁴² The break-in procedures consisted of a series of voltage cycles in the fuel cell

regime of 0.6–0.9 V. During the voltage recovery step, the cell is held under saturated conditions and low potentials of 0.1 V under H_2/air flow. This procedure has been previously described in detail.^{28,29} Voltage–current (V – I) measurements were performed at 80°C , 150/150 kPa, and 1.5/2 stoichiometric H_2/air flow rates at 100/100% RH. Data were collected starting from the highest total cell current density of $1.5 \text{ A}/\text{cm}^2$ down to $0.05 \text{ A}/\text{cm}^2$, followed by an open-circuit voltage (OCV) hold for 10 s.

Cyclic voltammetry (CV) measurements were performed on the single cell after the polarization curve tests using a Metrohm Autolab potentiostat. During the CV measurements, the anode and cathode were purged with H_2/N_2 at flow rates of 500/200 sccm, respectively. The anode and cathode were both at 150 kPa back-pressure and 100% RH, and the cell temperature was 80°C . The electrochemically active surface area (ECA) was calculated from CV curves via the following equation:³⁰ $ECA = Q_{\text{H}}/(m \times q_{\text{H}})$, where Q_{H} is the charge exchanged during the underpotential deposition of H atoms on Pt, m is the Pt loading amount, and q_{H} ($210 \text{ mC}/\text{cm}^2$) is the charge required for monolayer adsorption of H on Pt surfaces. Q_{H} was obtained by integrating the area in the H adsorption region of the CV after subtraction of the double-layer charge background.

Limiting current measurements were performed in 5 cm^2 differential hardware at 80°C and 75% RH, with oxygen mole fractions of 0.02, 0.03, and 0.05 at total cell pressures of 100, 150, 200, and 300 kPa. The limiting current was measured during constant voltage holds of 3 min duration at 0.30, 0.24, 0.18, 0.12, and 0.06 V. The total transport resistance (R_T) values were calculated from the limiting current densities and plotted as a function of pressure, and the pressure-independent non-Fickian transport resistance (R_{NF})

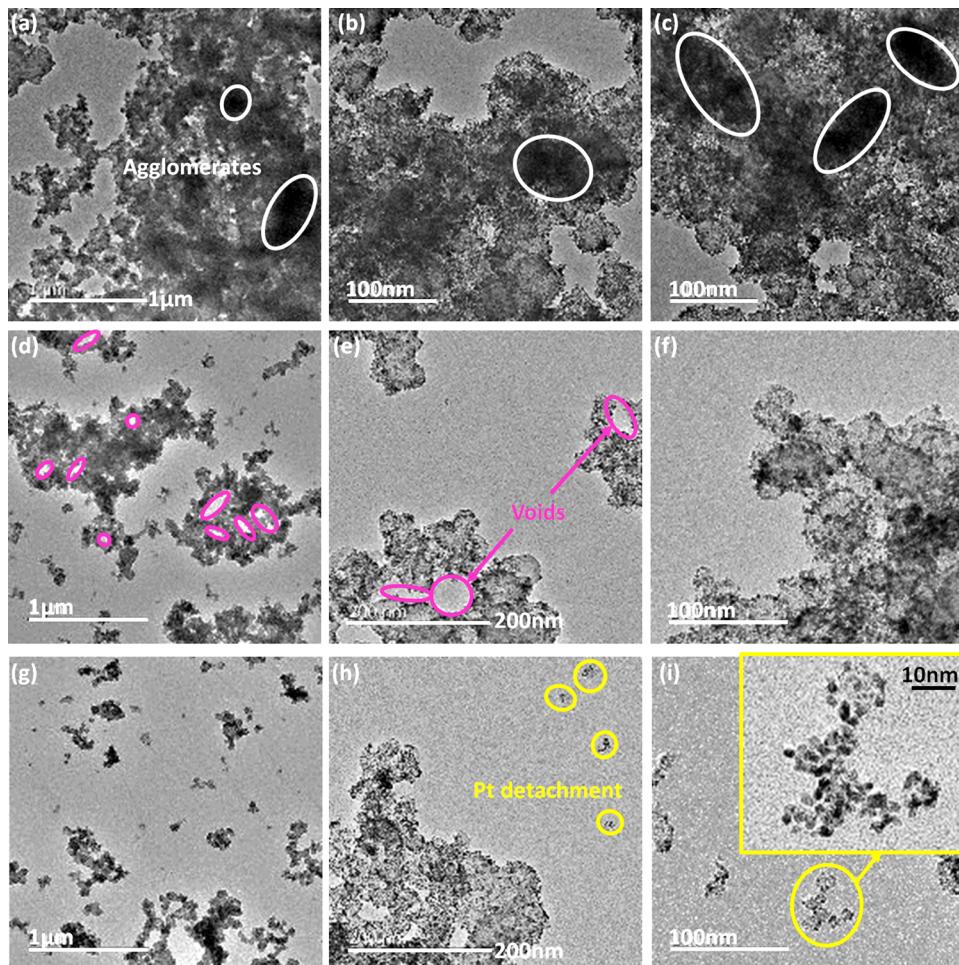


Figure 3. (a–c) TEM images of the catalyst ink with 1 min bath sonication under different magnifications. (d–f) TEM images of the catalyst ink with 10 s tip and 20 min bath sonication under different magnifications. (g–i) TEM images of the catalyst ink with 20 min tip sonication under different magnifications.

values were extracted from the plot's intercept. Additional details of this procedure have been previously described by Baker et al.³¹

3. RESULTS AND DISCUSSION

The breakup of agglomerates into primary aggregates is one of the key factors in electrode ink preparation to achieve a high fuel cell performance. These carbon agglomerates are easily formed due to the aggregation of catalyst–support particles and ionomer in the catalyst ink during the ink formulation process.³² As described in the [Experimental Section](#), data acquired on the USAXS–SAXS–WAXS instrument provides information about the dimensions and distributions of carbon and metal structures over a wide range of length scales. These range from the tens of nanometers to several micrometer sizes of carbon primary aggregates and fractal agglomerates (USAXS), nanometer size of catalyst particles (SAXS), and angstrom-level interatomic spacing of the catalyst particles and carbon support (WAXS). The USAXS regions of the scattering curves for the three different sonication methods are shown in [Figure 1a](#). The intensity data sets have been offset to overlap at $q = 0.02 \text{ \AA}^{-1}$ on the y -axis to clearly highlight the differences in curvature of these data sets.

The scattering vector (q) is inversely proportional to particle size and increasing intensity at a given q indicates a higher population of particles at that size. For all sonication methods,

with increasing sonication time the scattering intensities near $q = 0.001 \text{ \AA}^{-1}$ (carbon aggregates region) increase as the agglomerates break up into smaller aggregates, increasing the volume of scatters of this size ($\sim 100 \text{ nm}$). The power-law slope of the curves at low q ($< 0.0002 \text{ \AA}^{-1}$) decreases with sonication due to a decrease in the size of the agglomerates. The scattered X-ray intensity in this region arises from carbon agglomerates whose radius of gyration is beyond the measuring range of USAXS ($> 5 \mu\text{m}$).

As shown in [Figure 1b,c](#), the normalized intensity data clearly show a quick change in scattering after only 1 min of bath sonication and after 10 s of tip sonication and only subtle changes after that. All sonication methods reached a constant agglomerate and aggregate population after ≈ 10 min of sonication. Comparing the different sonication methodologies, tip sonication appears to be the most effective method at breaking up carbon agglomerates into aggregates, as indicated by the highest intensity at $q = 0.001 \text{ \AA}^{-1}$ and lowest intensity at $q = 0.0002 \text{ \AA}^{-1}$. It can be speculated that sonication power and time beyond that necessary to reach a steady-state breakup of agglomerates not only wastes time and energy but can also damage the catalyst, as suggested in prior RDE experiments.²⁰ We explore the effect of excessive sonication on ECA and fuel cell performance in the next section.

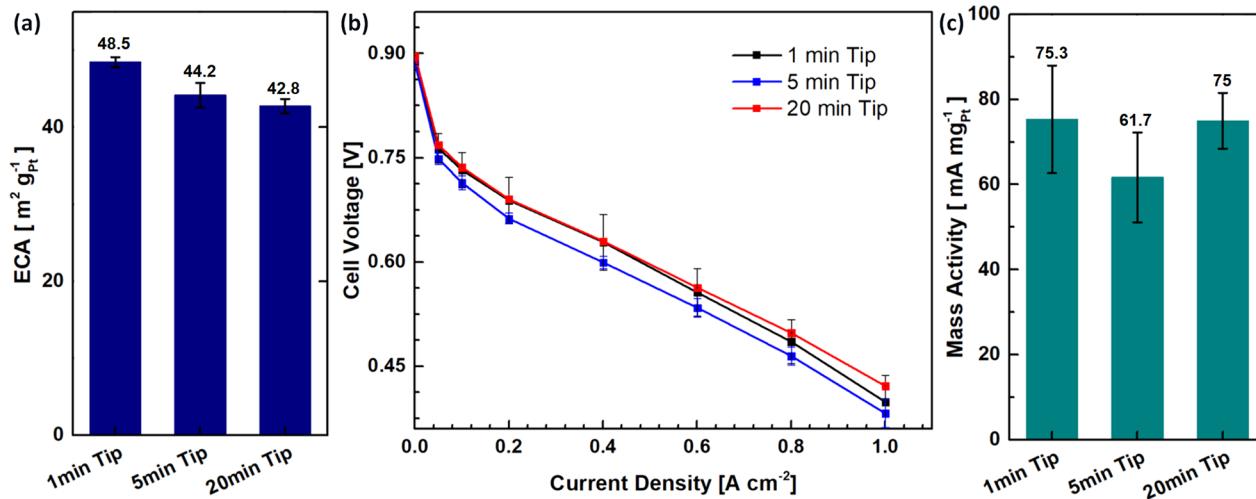


Figure 4. (a) ECA, (b) H_2/air polarization curves, and (c) ORR mass activity at 0.9 V (HFR and H_2 crossover corrected) of MEAs with cathode catalyst inks processed by tip sonication.

Figure 2 shows the WAXS data corresponding with the USAXS data shown in Figure 1, which shows the impact of sonication on the phase structure of the catalyst. While there is no change in the peak positions in the WAXS profiles, indicating that sonication does not affect the phase structure/atomic spacing of the catalyst, an increase in WAXS scattering intensity with sonication time is noted, especially of the Pt (111) peak. The increase in the intensity of the scattering peaks from the various atomic planes of Pt is caused by the breakup of the catalyst agglomerates and formation of a more spatially uniform dispersion which causes more of the Pt to be in the $0.8 \text{ mm} \times 0.2 \text{ mm}$ beam path within the 4 mm diameter glass tube. The lack of change of the width of the WAXS peaks and of the q value of the SAXS peak show that the Pt crystallites/particles are not increasing substantially in size with sonication. For the tip-only case, the peak intensity of Pt increases significantly after 1 min and stays constant for the remainder of the process. For the bath-only and tip/bath sonication methods the Pt peaks show a gradual increase in the intensity of the WAXS Pt peak area with sonication time.

To confirm the findings of the USAXS and WAXS measurements, TEM of dried inks was used to visualize the catalyst agglomerate size for inks subjected to a selected set of dispersing conditions. The TEM images were acquired for catalyst ink drop cast and dried on a TEM grid. Shown in Figure 3a–c are images of the ink after 1 min bath sonication. The dark areas marked by the white circles represent the large carbon agglomerates. In this case, most carbon black presented as large agglomerates. This is consistent with the USAXS and WAXS data in Figures 1 and 2, which show minimal agglomerate break-up after this brief and seemingly insufficient sonication period. This would be expected to hinder ionomer from accessing a large portion of the catalyst particles, resulting in a poor ionomer network and reduced three phase boundaries (TPBs). TPBs are the regions of contact between the catalysts, the electrolyte (ionomers), and the reactant gas (O_2).³³ The TPBs directly affect the cell performance including the reaction kinetics, mass activity, and overall performance.³⁴

In this regard, the desired CCL structure should have abundant TPBs for the ORR, which was the appropriate sonication case shown in Figure 3d,e. As can be seen, the

catalyst inks treated by 10 s tip and 20 min bath sonication exhibited smaller particle size compared to the insufficient sonication case. The large carbon agglomerates were broken down with increasing sonication time, and numerous voids, marked by pink circles, were observed. These voids suggest a better dispersion of the Pt/V aggregates. Moreover, the Pt nanoparticles (small black shapes) were uniformly distributed on the carbon black support as shown in Figure 3f. These images are also consistent with what was observed in the USAXS and WAXS analyses. These results show that this more appropriate sonication procedure breaks the large agglomerates into smaller primary aggregates.

The last dispersion condition examined with TEM was tip sonication for 20 min. The USAXS and WAXS showed that this tip sonication was the most effective method for breaking up agglomerates into primary aggregates. The TEM images in Figure 3g–i also show this. The TEM images of Figure 3h,i also show that many of the Pt nanoparticles were dislodged from the carbon black support. This indicates that this sonication is excessive and should lead to decreased cell performance as the detached particles will not be electronically accessible and will not be able to participate in the ORR. This would manifest itself as an observed decrease in ECA and MA.

To understand the relationship between catalyst agglomeration and performance, CCLs were prepared from the inks dispersed under the different ultrasonic dispersing conditions. These CCLs were used to prepare MEAs for in-situ electrochemical testing. The electrochemical performance of the tip only group is presented in Figure 4. Compared to bath sonication, tip sonication generates higher energy and is a more aggressive processing technique, as shown by the previous X-ray and TEM analysis. As can be seen in Figure 4a, the ECA decreased with increasing sonication time, which can be attributed to the detachment and aggregation of Pt nanoparticles based on correlation with the TEM results presented in Figure 3h,i. Overall, the MA and air performance of the tip only group were poor. In detail, the MEA fabricated from the ink sonicated for 1 min using the tip exhibited a reasonable ECA of $48.5 \text{ m}^2 \text{ g}^{-1}_{\text{Pt}}$ but a poor MA of $75.3 \text{ mA mg}^{-1}_{\text{Pt}}$. According to the USAXS data, only 1 min of tip sonication was effective at breaking up agglomerates as the intensity at $q = 0.0002 \text{ \AA}^{-1}$ is very low even after this limited

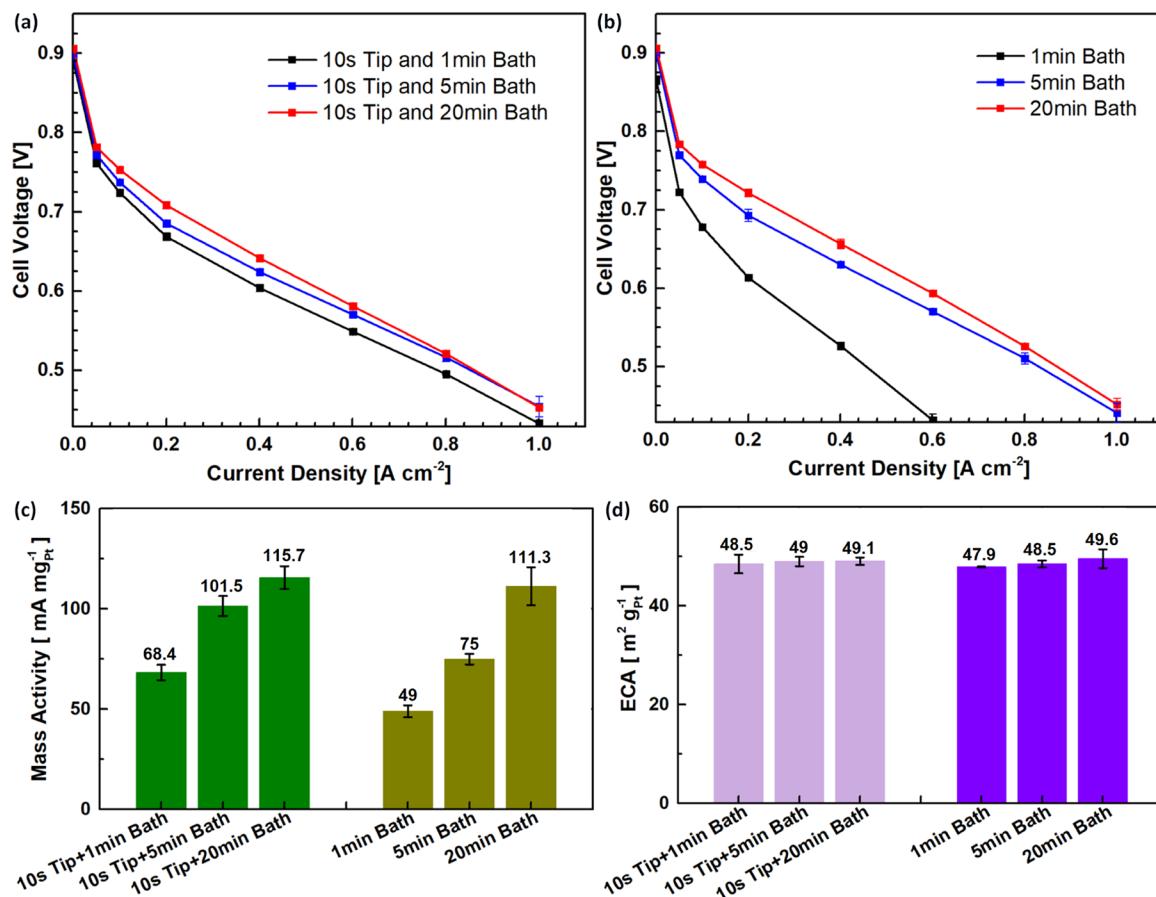


Figure 5. H_2/air polarization curves of MEAs with cathode catalyst inks processed by (a) combined sonication and (b) bath only sonication. (c). Mass activity and (d) ECA of MEAs with different ink processing.

sonication time. This would suggest the ink has been well dispersed; however, the low MA indicates that this sonication procedure is not sufficient for optimized MEA performance. A possibility is that some time-dependent behavior in the dispersing process affected the MA, which was not captured in X-ray scattering and is not understood yet.

With increasing sonication time, the carbon aggregates were further broken down; however, this did not lead to improvements in MEA performance. The ECA decreased as the electroactive Pt NPs were dislodged from the carbon supports. The USAXS data do not show significant change in agglomerate size between 5 and 20 min, but interestingly there was a slight enhancement of MA during this time. This would also support our previous supposition that sonication time may also be influencing how much ionomer is adsorbing onto the catalyst particles. Regardless, it was difficult to achieve the optimized processing condition in terms of resulting MEA performance for this aggressive sonication method.

Unlike the tip sonication, bath sonication was milder with a lower output power. The combined sonication group first applied 10 s tip sonication followed by bath sonication for the same treatment times as that of the bath only group. The H_2/air polarization curves and mass activities are presented in Figure 5a–c. Both sonication methodologies showed an obvious enhancement in the mass activity with increasing sonication time, as shown in Figure 5b. Initially there appears to be an advantage to including the 10 s tip sonication. Figure S2 compares the polarization curves and mass activity of the MEAs with and without 10 s tip sonication. For a limited bath

sonication time, such as 1 min, the 10 s tip sonication effectively improved the overall performance as well as the mass activity. The effect is also seen in Figure 5c as the mass activity starts higher and approaches its maximum faster with the tip sonication than without. This is also seen in air polarization curves in Figure 5a,b, as the cell potential at 1 A cm^{-2} increases faster with the initial tip sonication. These results are consistent with what was observed in the USAXS and WAXS measurements. In the combined sonication group, the first 10 s tip sonication was employed to break down the large particles, which was confirmed by USAXS as the inks with the 10 s tip sonication had more aggregates and fewer larger agglomerates than the ink without tip sonication. At these short sonication times, the brief tip sonication step allowed for more dispersed catalyst aggregates, which is why we observe improvements in mass activity and air performance.

Interestingly, when the bath sonication time reached 20 min, the extra tip sonication did not provide a significant benefit in mass activity or air performance. Both “10 s tip and 20 min bath” and “20 min bath” MEAs exhibited good electrochemical performance. These results are also consistent with the USAXS/WAXS analysis. We observe that by 15 min of bath sonication the scattering intensities at 0.001 and 0.0002 \AA^{-1} are the same regardless of whether or not the tip sonication was used. Similarly, the WAXS data in Figure 2 show that it is not until 20 min of bath sonication the inks have similar peak intensity. This indicates that at longer bath sonication time the initial tip sonication does not impact the catalyst agglomerate size.

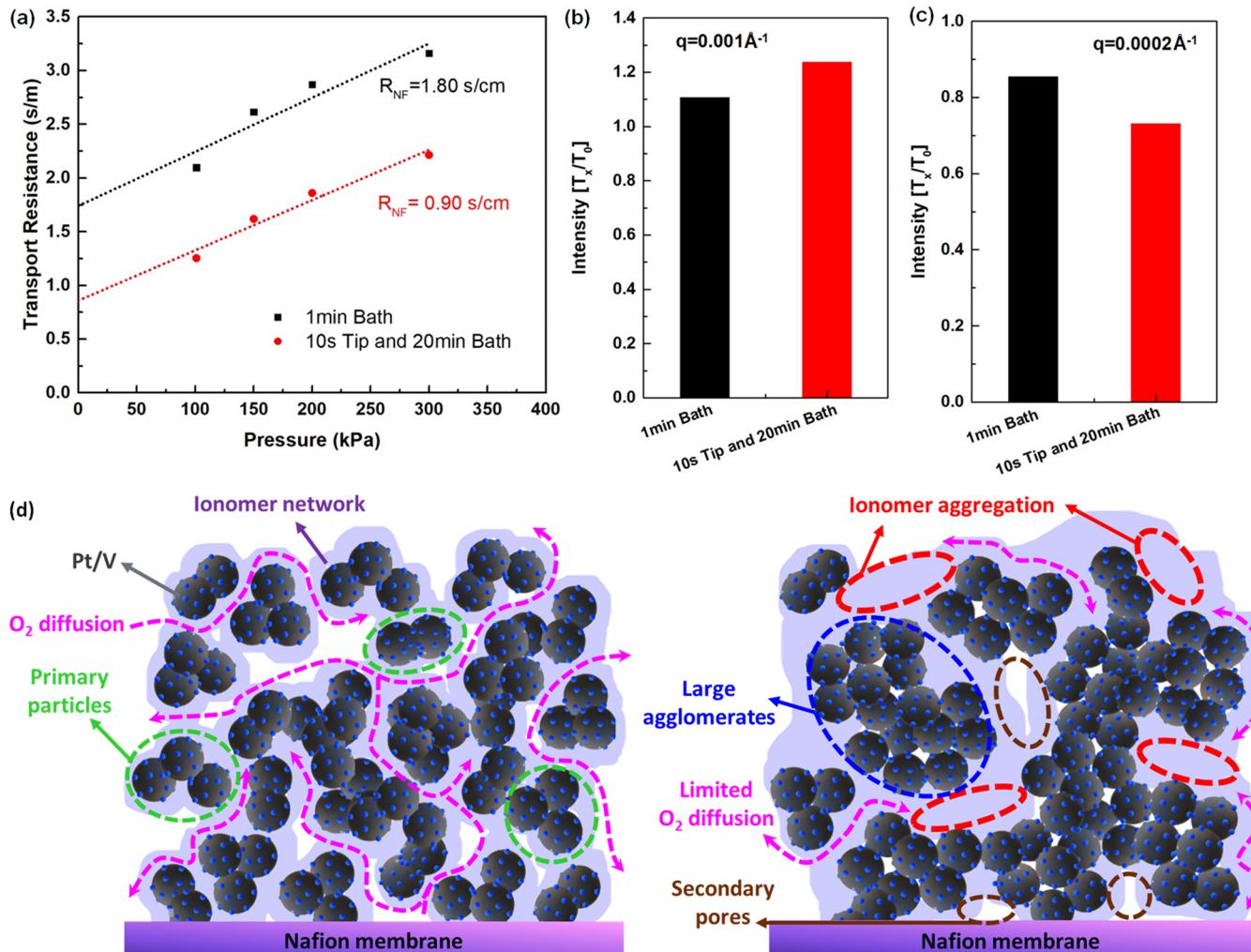


Figure 6. (a) Limiting current measurements of MEAs with catalyst inks processed by 1 min bath and 10 s tip and 20 min bath sonication. USAXS data of catalyst inks processed by 1 min bath and 10 s tip and 20 min bath sonication at the region of (b) $q = 0.001 \text{ Å}^{-1}$ and (c) $q = 0.0002 \text{ Å}^{-1}$. (d) Proposed cathode catalyst layer structure of MEA with 10 s tip and 20 min bath sonication (left) and 1 min bath sonication (right).

These results show the advantages of bath sonication to pure tip sonication. With appropriate sonication treatment such as “10 s tip and 20 min bath” and “20 min bath”, the large carbon agglomerates were broken down to small aggregates without losing Pt catalysts, and thus a better ionomer network and more TPBs were formed in the catalyst layer. As can be seen in Figure 5d, the ECAs of electrodes prepared by different conditions in the bath only and combined sonication groups were $48\text{--}49 \text{ m}^2 \text{ g}^{-1}_{\text{Pt}}$, confirming that the Pt NPs were not detached from the Vulcan carbon support.

Examining the air polarization curves in Figure 5, it can be seen that with increasing sonication time there is an improvement in the high-current density performance. As is well-known, the polarization curve at the high current densities is affected by mass transport of reactants to the catalytic sites. To further investigate the effect of catalyst particle size on the mass transport behavior, O₂ limiting current measurements were employed to evaluate pressure-dependent transport resistance.³¹ Through this methodology, the Fickian and non-Fickian O₂ resistances can be determined. Catalyst inks treated by 1 min bath (insufficient sonication case) and 10 s tip and 20 min bath (appropriate sonication case) were selected since they had very different polarization curves, especially at

the high current densities, suggesting differences in O₂ mass transport. Figure 6a presents the measured transport resistance as a function of pressure. Extrapolating the linear trendline to zero pressure estimates the non-Fickian (pressure-independent) O₂ transport resistance (R_{NF}).

Figure 6a shows that there was a significant reduction in RNF for the MEA that was fabricated with a catalyst ink that was appropriately sonicated ($R_{NF} = 0.90 \text{ s/cm}$) in comparison to the ink that was insufficiently sonicated ($R_{NF} = 1.80 \text{ s/cm}$). It has been previously established that non-Fickian transport resistances arise primarily from diffusion through small pores less than 100 nm in size, liquid water, and ionomer.³⁵ These measurements were conducted at slightly dry conditions (75% RH), so therefore R_{NF} through liquid water can be neglected. The differences in R_{NF} and overall fuel cell performance are most likely due to catalyst particle size and ionomer coverage on the surface of the Vulcan support. From the aspect of particle size, the measured scattering intensity from aggregates ($q = 0.001 \text{ Å}^{-1}$) and agglomerates ($q = 0.0002 \text{ Å}^{-1}$) are shown in Figures 6b and 6c, respectively. Figure 6d is the proposed cathode catalyst layer structure of the MEA with 1 min bath and 10 s tip and 20 min bath. Longer sonication time leads to more primary aggregates and fewer large agglomerates. Even

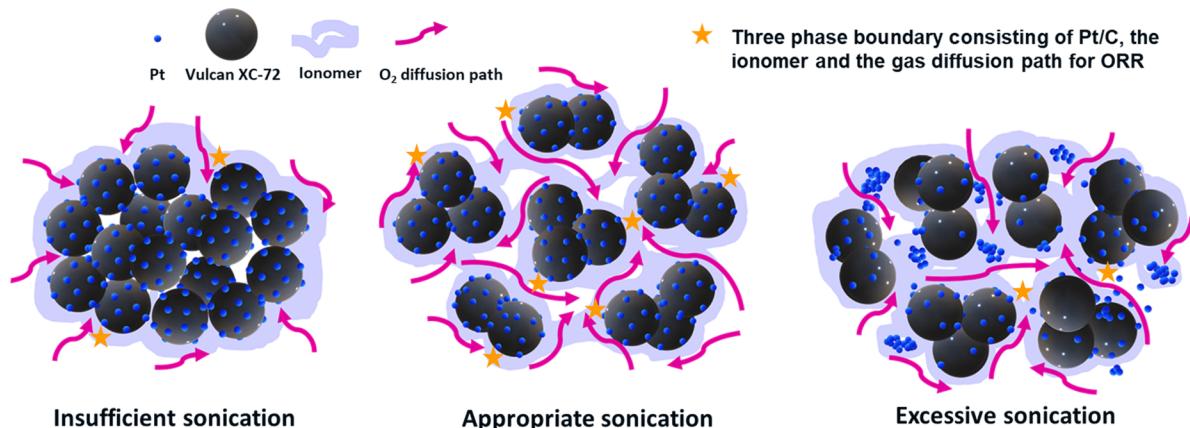


Figure 7. Proposed structure of Pt/C and Nafion ionomer with different ink processing.

though Pt/V carbon black particles do not have significant micropore volume (<2 nm), they do have a significant mesopore and macropore volume from the primary pores (2–20 nm) within an aggregate and secondary pores (20–100 nm) between aggregates in larger agglomerates.^{12,36} These pore sizes are small enough to be in the non-Fickian regime or at least transitional regime between Fickian and non-Fickian and would give rise to non-Fickian O_2 transport resistance as the O_2 diffuses through the electrode to reach Pt sites. Large agglomerates (1 min bath) will have more secondary pores between aggregates than more well-dispersed aggregates (10 s tip and 20 min bath). This increase in pores lead to a higher resistance for O_2 diffusing to Pt particles in the center of large agglomerates. These secondary pores will be decreased as the large agglomerates are broken down leading to the decrease in non-Fickian O_2 resistance that was observed in our measurements.

Moreover, the particle size distribution will also affect the ionomer arrangement and thus change the R_{NF} . Larger agglomerates will have a lower surface area-to-volume ratio than smaller agglomerates/aggregates. This may lead to the a thicker Nafion film covering the agglomerates. It is well established that the O_2 transport resistance through the ionomer film is a component of R_{NF} .^{37–40} Agglomerate model results have shown that as ionomer film thickness increases with increasing aggregate radius the limiting current decreases due to increased ionomer film resistance.⁴¹ This increased ionomer film resistance would lead to the increase in R_{NF} that we observe in our measurements.

Based on our experimental results, three dispersed states of catalyst particles are proposed. Illustrations of these structures are shown in Figure 7. First, with insufficient sonication, the primary aggregates remain highly agglomerated. As a result, ionomer only coats the exterior of the agglomerates, and thus the interior Pt particles are not accessible to protons, leading to the lower mass activities that were observed (Figure 5c). This structure also results in higher O_2 mass transport resistance due to more secondary pores, as is shown in Figure 6d. The second case is appropriate sonication. In this case large agglomerates were successfully broken down to the smaller aggregates. This allows the ionomer to be more uniformly distributed on the aggregates, resulting in better catalyst utilization. Also, reagent gases have lower resistance to access the catalyst materials due to fewer secondary pores. The final case is excessive sonication. Here the agglomerates were effectively broken down; however, the process is overly

aggressive, and Pt NPs are detached from the carbon black support. This renders particles unable to participate in ORR resulting in lower ECA and mass activity.

4. CONCLUSION

This work demonstrates the combined USAXS–SAXS–WAXS as a powerful in-situ technique to study the dispersion of fuel cell catalyst inks. Combined with TEM and in-situ electrochemical testing, we were able to directly correlate catalyst agglomeration to fuel cell performance. A 10 s tip plus 20 min bath sonication was demonstrated to be an efficient way to break down carbon agglomerates into primary particles without detaching the Pt NPs. This allows the ionomer to be more uniformly distributed on the aggregates, resulting in better catalyst utilization. Primary particles remained highly agglomerated when insufficient sonication was used, which limited the accesses of interior Pt NPs to ionomers, resulting in poor mass activities and performance. With excessive sonication, Pt NPs detachment was serious and thus decreasing the ECA and poor ORR performance. Utilizing oxygen limiting current measurements, we were able to show that catalyst agglomerate size influences non-Fickian oxygen transport resistance. These results further support previous reports showing the importance of properly dispersing catalyst inks to maximize performance. Moving forward these results provide a foundation to understand catalyst agglomerates behavior and fuel cell performance in different ink formulations (solvent systems and concentrations) and when using different dispersing methods.

■ ASSOCIATED CONTENT

Supporting Information

The Supporting Information is available free of charge on the ACS Publications website at DOI: 10.1021/acsaem.9b01037.

Experimental setup of the ink circulation at the X-ray beamline hutch; air polarization curves and mass activity of MEAs with catalyst inks processed by different sonication time; performance summarization of the MEAs with different cathode catalyst ink processing; Figure S1: experimental setup of the ink circulation at the X-ray beamline hutch; Figure S2: air polarization curves of MEAs with catalyst inks processed by different sonication times: (a) 1 min, (b) 5 min, and (c) 20 min; (d) mass activity comparison of MEAs with catalyst inks processed by different sonication time; Table S1:

performance summarization of the MEAs with different cathode catalyst ink processing ([PDF](#))

AUTHOR INFORMATION

Corresponding Author

*E-mail: scott.mauger@nrel.gov.

ORCID

Min Wang: [0000-0002-5051-9199](#)

K. C. Neyerlin: [0000-0002-6753-9698](#)

Scott A. Mauger: [0000-0003-2787-5029](#)

Author Contributions

†M.W. and J.H.P. contributed equally to this work.

Notes

The authors declare no competing financial interest.

ACKNOWLEDGMENTS

The authors thank Jan Ilavsky and Ivan Kuzmenko of APS 9-ID for assistance with USAXS measurements. This work was authored in part by Alliance for Sustainable Energy, LLC, the manager and operator of the National Renewable Energy Laboratory for the U.S. Department of Energy (DOE) under Contract DE-AC36-08GO28308. Funding was provided by U.S. Department of Energy Office of Energy Efficiency and Renewable Energy Advanced Manufacturing Office, Program Manager David Hardy. The submitted manuscript was created, in part, by U Chicago Argonne, LLC, Operator of Argonne National Laboratory, Argonne, U.S. Department of Energy Office of Science laboratory, operated under Contract DE-AC02-06CH11357. This research used the resources of the Advanced Photon Source (APS), a U.S. Department of Energy (DOE) Office of Science User Facility, operated for the DOE Office of Science by Argonne National Laboratory, also under Contract DE-AC02 06CH11357. The views expressed in the article do not necessarily represent the views of the DOE or the U.S. Government. The U.S. Government retains and the publisher, by accepting the article for publication, acknowledges that the U.S. Government retains a nonexclusive, paid-up, irrevocable, worldwide license to publish or reproduce the published form of this work, or allow others to do so, for U.S. Government purposes.

REFERENCES

- (1) Banham, D.; Ye, S. Current Status and Future Development of Catalyst Materials and Catalyst Layers for Proton Exchange Membrane Fuel Cells: An Industrial Perspective. *ACS Energy Lett.* **2017**, *2* (3), 629–638.
- (2) Mauger, S. A.; Neyerlin, K. C.; Alia, S. M.; Ngo, C.; Babu, S. K.; Hurst, K. E.; Pylypenko, S.; Litster, S.; Pivovar, B. S. Fuel Cell Performance Implications of Membrane Electrode Assembly Fabrication with Platinum-Nickel Nanowire Catalysts. *J. Electrochem. Soc.* **2018**, *165* (3), F238–F245.
- (3) Litster, S.; McLean, G. PEM Fuel Cell Electrodes. *J. Power Sources* **2004**, *130*, 61–76.
- (4) O’Hayre, R.; Cha, S.-W.; Colella, W.; Prinz, F. B. *Fuel Cell Fundamentals*, 3rd ed.; Wiley: 2005.
- (5) Millington, B.; Whipple, V.; Pollet, B. G. A Novel Method for Preparing Proton Exchange Membrane Fuel Cell Electrodes by the Ultrasonic-Spray Technique. *J. Power Sources* **2011**, *196* (20), 8500–8508.
- (6) Erkan, S.; Eroglu, I. Ultrasonic Spray Coating Technique for High-Performance PEM Fuel Cell Electrode Manufacturing. *Progress in Clean Energy* **2015**, *2*, 481–492.
- (7) Lobato, J.; Rodrigo, M. A.; Linares, J. J.; Scott, K. Effect of the Catalytic Ink Preparation Method on the Performance of High Temperature Polymer Electrolyte Membrane Fuel Cells. *J. Power Sources* **2006**, *157* (1), 284–292.
- (8) Mauger, S. A.; Neyerlin, K. C.; Yang-Neyerlin, A. C.; More, K. L.; Ulsh, M. Gravure Coating for Roll-to-Roll Manufacturing of Proton-Exchange-Membrane Fuel Cell Catalyst Layers. *J. Electrochem. Soc.* **2018**, *165* (11), F1012–F1018.
- (9) Pollet, B. G. The Use of Ultrasound for the Fabrication of Fuel Cell Materials. *Int. J. Hydrogen Energy* **2010**, *35* (21), 11986–12004.
- (10) Xu, H.; Brosha, E. L.; Garzon, F. H.; Uribe, F.; Wilson, M.; Pivovar, B. The Effect of Electrode Ink Processing and Composition on Catalyst Utilization. *ECS Trans.* **2007**, *11* (1), 383–391.
- (11) Khandavalli, S.; Park, J. H.; Kariuki, N. N.; Myers, D. J.; Stickel, J. J.; Hurst, K.; Neyerlin, K. C.; Ulsh, M.; Mauger, S. A. Rheological Investigation on the Microstructure of Fuel Cell Catalyst Inks. *ACS Appl. Mater. Interfaces* **2018**, *10* (50), 43610–43622.
- (12) Soboleva, T.; Zhao, X.; Malek, K.; Xie, Z.; Navessin, T.; Holdcroft, S. On the Micro-, Meso-, and Macroporous Structures of Polymer Electrolyte Membrane Fuel Cell Catalyst Layers. *ACS Appl. Mater. Interfaces* **2010**, *2* (2), 375–384.
- (13) Long, C. M.; Nasarella, M. A.; Valberg, P. A. Carbon Black vs. Black Carbon and Other Airborne Materials Containing Elemental Carbon: Physical and Chemical Distinctions. *Environ. Pollut.* **2013**, *181*, 271–286.
- (14) Khan, Z. U.; Kausar, A.; Ullah, H. A Review on Composite Papers of Graphene Oxide, Carbon Nanotube, Polymer/GO, and Polymer/CNT: Processing Strategies, Properties, and Relevance. *Polym.-Plast. Technol. Eng.* **2016**, *55* (6), 559–581.
- (15) Holdcroft, S. Fuel Cell Catalyst Layers: A Polymer Science Perspective. *Chem. Mater.* **2014**, *26* (1), 381–393.
- (16) Malek, K.; Mashio, T.; Eikerling, M. Microstructure of Catalyst Layers in PEM Fuel Cells Redefined: A Computational Approach. *Electrocatalysis* **2011**, *2*, 141–157.
- (17) Ryu, J. G.; Lee, J. W.; Kim, H. Development of Poly(Methyl Methacrylate)-Clay Nanocomposites by Using Power Ultrasonic Wave. *Macromol. Res.* **2002**, *10* (4), 187–193.
- (18) Pollet, B. G.; Goh, J. T. E. The Importance of Ultrasonic Parameters in the Preparation of Fuel Cell Catalyst Inks. *Electrochim. Acta* **2014**, *128*, 292–303.
- (19) Pollet, B. G. Let’s Not Ignore the Ultrasound Effects on the Preparation of Fuel Cell Materials. *Electrocatalysis* **2014**, *5*, 330–343.
- (20) Shinozaki, K.; Zack, J. W.; Richards, R. M.; Pivovar, B. S.; Kocha, S. S. Oxygen Reduction Reaction Measurements on Platinum Electrocatalysts Utilizing Rotating Disk Electrode Technique. *J. Electrochem. Soc.* **2015**, *162* (10), F1144–F1158.
- (21) Pabisch, S.; Feichtenschlager, B.; Kickelbick, G.; Peterlik, H. Effect of Interparticle Interactions on Size Determination of Zirconia and Silica Based Systems - A Comparison of SAXS, DLS, BET, XRD and TEM. *Chem. Phys. Lett.* **2012**, *521*, 91–97.
- (22) Ilavsky, J.; Jemian, P. R.; Allen, A. J.; Zhang, F.; Levine, L. E.; Long, G. G. Ultra-Small-Angle X-Ray Scattering at the Advanced Photon Source. *J. Appl. Crystallogr.* **2009**, *42*, 469–479.
- (23) Yang, F.; Xin, L.; Uzunoglu, A.; Qiu, Y.; Stanciu, L.; Ilavsky, J.; Li, W.; Xie, J. Investigation of the Interaction between Nafion Ionomer and Surface Functionalized Carbon Black Using Both Ultrasmall Angle X-Ray Scattering and Cryo-TEM. *ACS Appl. Mater. Interfaces* **2017**, *9* (7), 6530–6538.
- (24) Papadias, D. D.; Ahluwalia, R. K.; Kariuki, N.; Myers, D.; More, K. L.; Cullen, D. A.; Snead, B. T.; Neyerlin, K. C.; Mukundan, R.; Borup, R. L. Durability of Pt-Co Alloy Polymer Electrolyte Fuel Cell Cathode Catalysts under Accelerated Stress Tests. *J. Electrochem. Soc.* **2018**, *165* (6), F3166–F3177.
- (25) Ilavsky, J.; Jemian, P. R. Irena: Tool Suite for Modeling and Analysis of Small-Angle Scattering. *J. Appl. Crystallogr.* **2009**, *42*, 347–353.
- (26) Kongkanand, A.; Mathias, M. F. The Priority and Challenge of High-Power Performance of Low-Platinum Proton-Exchange Membrane Fuel Cells. *J. Phys. Chem. Lett.* **2016**, *7* (7), 1127–1137.

- (27) Padgett, E.; Andrejevic, N.; Liu, Z.; Kongkanand, A.; Gu, W.; Moriyama, K.; Jiang, Y.; Kumaraguru, S.; Moylan, T. E.; Kukreja, R.; Muller, D. A. Editors' Choice—Connecting Fuel Cell Catalyst Nanostructure and Accessibility Using Quantitative Cryo-STEM Tomography. *J. Electrochem. Soc.* **2018**, *165* (3), F173–F180.
- (28) Kabir, S.; More, K. L.; Myers, D. J.; Kariuki, N.; Kropf, A. J.; Cetinbas, F.; Park, J.; Macauley, N.; Pan, Y.-T.; Mukundan, R.; Spendelow, J. S.; Borup, R. L.; Neyerlin, K. C. Investigating the Influence of MEA Conditioning on Commercial Pt/C and State-of-the-Art Pt-Alloy/C Electrocatalysts in a PEMFC. *ECS Meet. Abstr.* **2018**, No. 44, 1517–1517.
- (29) Zhang, J.; Paine, L. Methods and Processes to Recover Voltage Loss of Pem Fuel Cell Stack. US20110195324A1, 2011.
- (30) Stevens, D. A.; Dahn, J. R. Electrochemical Characterization of the Active Surface in Carbon-Supported Platinum Electrocatalysts for PEM Fuel Cells. *J. Electrochem. Soc.* **2003**, *150* (6), A770–A775.
- (31) Baker, D. R.; Caulk, D. A.; Neyerlin, K. C.; Murphy, M. W. Measurement of Oxygen Transport Resistance in PEM Fuel Cells by Limiting Current Methods. *J. Electrochem. Soc.* **2009**, *156* (9), B991–B1003.
- (32) Shukla, S.; Bhattacharjee, S.; Weber, A. Z.; Secanell, M. Experimental and Theoretical Analysis of Ink Dispersion Stability for Polymer Electrolyte Fuel Cell Applications. *J. Electrochem. Soc.* **2017**, *164* (6), F600–F609.
- (33) O'Hayre, R.; Barnett, D. M.; Prinz, F. B. The Triple Phase Boundary. *J. Electrochem. Soc.* **2005**, *152* (2), A439–A444.
- (34) Zhang, J. *PEM Fuel Cell Electrocatalysts and Catalyst Layers: Fundamentals and Applications*; Springer: London, 2008.
- (35) Huang, J.; Li, Z.; Zhang, J. Review of Characterization and Modeling of Polymer Electrolyte Fuel Cell Catalyst Layer: The Blessing and Curse of Ionomer. *Frontiers in Energy* **2017**, *11* (3), 334–364.
- (36) Uchida, M. Investigation of the Microstructure in the Catalyst Layer and Effects of Both Perfluorosulfonate Ionomer and PTFE-Loaded Carbon on the Catalyst Layer of Polymer Electrolyte Fuel Cells. *J. Electrochem. Soc.* **1995**, *142* (12), 4143–4149.
- (37) Xie, Z.; Navessin, T.; Zhao, X.; Adachi, M.; Holdcroft, S.; Mashio, T.; Ohma, A.; Shinohara, K. Nafion Ionomer Aggregation and Its Influence on Proton Conduction and Mass Transport in Fuel Cell Catalyst Layers. *ECS Trans.* **2008**, *16* (2), 1811–1816.
- (38) Weber, A. Z.; Kusoglu, A. Unexplained Transport Resistances for Low-Loaded Fuel-Cell Catalyst Layers. *J. Mater. Chem. A* **2014**, *2*, 17207–17211.
- (39) Owejan, J. P.; Owejan, J. E.; Gu, W. Impact of Platinum Loading and Catalyst Layer Structure on PEMFC Performance. *J. Electrochem. Soc.* **2013**, *160* (8), F824–F833.
- (40) Nonoyama, N.; Okazaki, S.; Weber, A. Z.; Ikogi, Y.; Yoshida, T. Analysis of Oxygen-Transport Diffusion Resistance in Proton-Exchange-Membrane Fuel Cells. *J. Electrochem. Soc.* **2011**, *158* (4), B416–B423.
- (41) Li, S.; Yuan, J.; Xie, G.; Sundén, B. Effects of Agglomerate Model Parameters on Transport Characterization and Performance of PEM Fuel Cells. *Int. J. Hydrogen Energy* **2018**, *43* (17), 8451–8463.
- (42) Kabir, S.; Myers, D. J.; Kariuki, N.; Park, J.; Wang, G.; Baker, A.; Macauley, N.; Mukundan, R.; More, K. L.; Neyerlin, K. C. Elucidating the Dynamic Nature of Fuel Cell Electrodes as a Function of Conditioning: An Ex-situ Materials Characterization and In-situ Electrochemical Diagnostic Study. Submitted to *ACS Appl. Mater. Interfaces*.

■ NOTE ADDED AFTER ASAP PUBLICATION

This paper was published on the Web on August 8, 2019, with co-author Min Wang incorrectly identified as a corresponding author. This was rectified, and the corrected version was reposted on August 16, 2019. A missing reference was identified and inserted, and this corrected version was reposted on August 29, 2019.